

FAST HIGH-DIMENSIONAL NODE GENERATION WITH VARIABLE DENSITY

O. VLASIUK, T. MICHAELS, N. FLYER, AND B. FORNBERG

ABSTRACT. We present an algorithm for producing discrete distributions with a prescribed nearest-neighbor distance function. Our approach is a combination of quasi-Monte Carlo methods and weighted Riesz energy minimization: the initial distribution is a stratified QMC sequence with some modifications; a suitable energy functional on the configuration space is then minimized to ensure local regularity. The resulting node sets are good candidates for building meshless solvers and interpolants, as well as for other applications where a point cloud with a controlled separation-covering ratio is required.

1. INTRODUCTION

1.1. RBFs and meshless methods. In a number of important applications, usefulness of meshless methods in general, and of radial basis functions (RBFs) in particular, is well-known. They have found their way into high-dimensional interpolation, machine learning, spectral methods, vector-valued approximation and interpolation, just to name a few [28], [9], [13], [7], [25]. RBFs have demonstrated having a number of advantages, most importantly extreme flexibility in forming stencils (in the case of RBF-FD) and high local adaptivity; allowing spectral accuracy on irregular domains; the fact that the corresponding interpolation matrix (denoted by \mathbf{A} below) is positive-definite for several types of radial functions and does not suffer from instability phenomena characteristic of some of the alternative interpolation methods.

Applying RBF-FD stencils to building solvers requires an efficient way of distributing the centers of basis elements in the domain, which can be either a solid or a surface. The tasks of modeling and simulation often call for distribution of massive numbers of RBF centers, which we will call *nodes*, so it is important to ensure that the distribution process is easily scalable. One further has to be able to place nodes according to a certain density, as a method of local refinement, for example, at the boundary, or in regions of special interest. Yet another challenge arises when it is necessary to deal with complex or non-smooth domains and/or surfaces.

Recall [14] that an RBF is a linear combination of the form

$$(1) \quad s(\mathbf{x}) = \sum_{i=1}^N w_i \phi(\|\mathbf{x} - \mathbf{x}_i\|),$$

where $\phi(\cdot)$ is a radial function, and \mathbf{x}_i , $i = 0 \dots, N$ is a collection of pairwise distinct points in \mathbb{R}^d . A common choice of ϕ is the Gaussian $\phi(r) = e^{-(\epsilon r)^2}$, although one may also use $1/(1 + (\epsilon r)^2)$, $r^{2p} \log(r)$, $p \in \mathbb{N}$, or any kernel approximating the delta-function [22]. In this discussion, we are not

Date: May 2, 2022.

Key words and phrases. Quasi-uniformity, irrational lattice, quasi-Monte Carlo methods, Riesz energy, gradient descent, separation distance, nearest neighbors.

concerned with the distinctions between the different radial kernels, so the reader should assume that $\phi(r) = e^{-(\epsilon r)^2}$. It is well-known that the matrix

$$\mathbf{A} = \begin{bmatrix} \phi(\|\mathbf{x}_1 - \mathbf{x}_1\|) & \phi(\|\mathbf{x}_1 - \mathbf{x}_2\|) & \dots & \phi(\|\mathbf{x}_1 - \mathbf{x}_N\|) \\ \phi(\|\mathbf{x}_2 - \mathbf{x}_1\|) & \phi(\|\mathbf{x}_2 - \mathbf{x}_2\|) & \dots & \phi(\|\mathbf{x}_2 - \mathbf{x}_N\|) \\ \vdots & \vdots & & \vdots \\ \phi(\|\mathbf{x}_N - \mathbf{x}_1\|) & \phi(\|\mathbf{x}_N - \mathbf{x}_2\|) & \dots & \phi(\|\mathbf{x}_N - \mathbf{x}_N\|) \end{bmatrix}$$

is positive-definite if the nodes $\mathbf{x}_1 \dots \mathbf{x}_N$ are all distinct, and therefore under this assumption there exists an n -point RBF interpolant for any function data. A different question, however, is whether the matrix \mathbf{A} will be well-conditioned: it is not the case, for example, when the nodes are placed on a lattice and $\epsilon \rightarrow 0$, [16]. It is due to this phenomenon that planar lattice nodes perform much worse than Halton nodes [16], or the quasi-uniform nodes constructed by the third and fourth authors [15]. Furthermore, node clumping can lead to instability of PDE solvers, [13]. To avoid this, one must guarantee that the RBF centers are separated.

In many applications, one has to ensure that the distance from a node \mathbf{x} to its nearest neighbor behaves approximately as a function of the position of the node [15]. Prescribing this function, $\rho(\mathbf{x})$, which we call the *radial density*, is a natural way to treat the cases when a local refinement is required in order to capture special features of the domain. In the present paper we will describe a method of node placement for which the actual distance to the nearest neighbor, denoted by $\Delta(\mathbf{x}) = \min_{\mathbf{x}' \neq \mathbf{x}} \|\mathbf{x}' - \mathbf{x}\|$, satisfies the above description. To summarize, we are interested in a procedure for obtaining discrete configurations inside a compact set that would:

- guarantee that $\Delta(\mathbf{x}) \asymp \rho(\mathbf{x})$ (that is, differ only up to a constant factor) for a given function $\rho(\mathbf{x})$ with a reasonably wide choice of ρ ;
- be suitable for mesh-free PDE discretizations using RBFs, i.e., produce well-separated configurations without significant node alignment;
- result in regular node distribution on the surface boundaries of the domain;
- be computationally efficient, easily scalable, and suitable for parallelization.

1.2. Notation and layout. The bold typeface is reserved for vectors in \mathbb{R}^d . With few exceptions, letters of the Greek alphabet denote functions, calligraphic letters and Ω denote sets, and the regular Roman typeface is used for scalar variables. The symbolic notation employed throughout the paper is summarized in Table 1.

The paper is structured as follows: Sections 2.1 and 2.2 introduce the two essential components of our approach, Riesz energy functionals and quasi-Monte Carlo methods. Sections 3.1 and 3.2 contain the description of the main algorithm, and its discussion, respectively. Sections 4.1-4.3 offer applications of the algorithm, and Section 5 contains the final remarks. The Appendix is dedicated to numerical experiments with the mean and minimal separation distance of Riesz minimizers and irrational lattices.

2. CHOICE OF METHOD

2.1. Riesz energy. To generate nodes both devoid of lattice alignment and having near-optimal local separation, we apply the energy minimization technique. Let us first introduce the *Riesz s -energy* of a collection $\mathbf{x}_1, \dots, \mathbf{x}_N$ as

$$(2) \quad E_s(\{\mathbf{x}_1, \dots, \mathbf{x}_N\}) = \sum_{i \neq j} \frac{1}{\|\mathbf{x}_i - \mathbf{x}_j\|^s}.$$

Symbol	Description
\bar{x}	mean value of x
$\alpha_1, \alpha_2, \dots, \alpha_{d-1}$	fixed linearly independent irrational numbers
\mathcal{C}	unit cube $[0, 1]^d$
C_1, C_2	positive constants in (5) and (7)
\mathbf{c}_m	the closest to the origin corner of \mathcal{V}_m
$\chi(\cdot; \Omega)$	characteristic function of the set Ω
\mathcal{D}	$m \in \mathcal{D}$ if \mathcal{V}_m has nonempty neighbors on Step 1
$\Delta(\mathbf{x})$	distance from the node \mathbf{x} to the nearest neighbor
$\Delta(\{\mathbf{x}_1, \dots, \mathbf{x}_N\})$	separation of the configuration
$\Delta^k(\mathbf{x}), k = 1, \dots, K$	distance from \mathbf{x} to the k -th nearest neighbor
Δ_n	minimal separation of periodized $\mathcal{L}_n, \mathcal{M}_n$, p. 6
$\bar{\Delta}_n$	mean separation of the periodized $\mathcal{L}_n, \mathcal{M}_n$, p. 6
\mathcal{E}	$m \in \mathcal{E}$ if \mathcal{V}_m is empty on Step 3
E_s, E_s^κ	Riesz s -energy and weighted s -energy, (2)-(3)
$\text{frac}(x)$	fractional part of the nonnegative number x
\mathcal{H}_d	d -dimensional Hausdorff measure
κ	kernel of the weighted Riesz energy, (3)
λ	interpolated inverse of $\bar{\Delta}_n$, p. 6
$\mathcal{L}_n, n \geq 1$	n -point irrational lattice, (5)
$\mathcal{M}_n, n \geq 1$	n -point periodic Riesz minimizer, p. 5
$\mathcal{L}'_n, \mathcal{M}'_n$	translated and rescaled \mathcal{L}_n and \mathcal{M}_n , (8)-(9)
n_m	number of nodes in \mathcal{V}_m
Ω	target distribution support
$\Omega_{\text{etopo}}, \Omega_{\text{shell}}$	the underlying sets in Sections 4.1 and 4.3
(r, a, p)	spherical coordinates, p. 9
$\rho(\mathbf{x})$	objective radial density, pp. 2, 5
$\mathcal{V}_m, m = 1, \dots, M^d$	cube-shaped voxel in \mathbb{R}^d , p. 4
$\mathbf{x}; \mathbf{x}_i, i = 1, \dots, N$	points in \mathbb{R}^d ; nodes of the configuration
\mathbf{z}_m	center of \mathcal{V}_m

TABLE 1. Symbolic notation employed throughout the paper.

There exists extensive literature dedicated to this and derived functionals for the case $s \geq d$, see in particular [17], [4], [18], where the limiting distribution of the minimizers of (2) is discussed, and additional multiplicative and additive weights are introduced. The *weighted Riesz s -energy* is defined in [4] as

$$(3) \quad E_s^\kappa(\{\mathbf{x}_1, \dots, \mathbf{x}_N\}) = \sum_{i \neq j} \frac{\kappa(\mathbf{x}_i, \mathbf{x}_j)}{\|\mathbf{x}_i - \mathbf{x}_j\|^s}.$$

It was proved [4], that the counting measures of the minimizers of (3) converge to $\kappa(\mathbf{x}, \mathbf{x})^{-d/s} d\mathcal{H}_d(\mathbf{x})$, where \mathcal{H}_d denotes the d -dimensional Hausdorff measure. It will be useful to assume that the weight function in (3) is chosen so that all the terms, except when \mathbf{x}_j is among the K nearest nodes to \mathbf{x}_i , are zero, a condition equivalent to truncated weights in [5]. As described in detail in [5], such

truncated kernel has the same energy asymptotics and limiting distribution, yet can be computed in the amount of time of order $O(NK)$, unlike the $O(N^2)$ order computation time for the complete kernel. The configurations which minimize this functional over n -point subsets of a compact set are well-separated, that is, the quantity $\Delta(\{\mathbf{x}_1, \dots, \mathbf{x}_N\}) = \min_i \Delta(\mathbf{x}_i)$ satisfies

$$(4) \quad \Delta(\{\mathbf{x}_1, \dots, \mathbf{x}_N\}) \geq CN^{-1/d}.$$

for all N . The value of the exponent s is chosen so that $s \geq d$ to ensure that the energy functional is sufficiently repulsive; it is known from the classical potential theory that for $s < d$ the minimal energy configurations are not necessarily uniform, and their local structure depends on the shape of the domain [20]. Property (4) holds for any $s > d$, when minimizing the energy over any fixed compact set $\Omega \subset \mathbb{R}^d$. While any symmetric kernel that grows fast enough towards the diagonal of $\Omega \times \Omega$ and smooth away from it would produce similar results, we chose the Riesz kernel because the properties of its minimizers are well understood.

Note that simply looking for minimizers of the weighted Riesz s -energy doesn't provide node sets satisfying $\Delta(\mathbf{x}) \asymp \rho(\mathbf{x})$; in fact, boundary nodes of such minimizers will often have smaller separations than desired. Since in such cases the boundary has a lower Hausdorff dimension, it does not influence the volumetric density, which agrees with the results above. With this motivation in mind, we are ready to introduce the second component of our method.

2.2. Quasi-Monte Carlo methods. To facilitate convergence of whichever optimization algorithm is used to find minimizers of (3), we can initialize it with a configuration that approximates the limiting measure. Due to the separation requirement, one has to rule out Monte Carlo method, as random points exhibit clustering [6], and turn instead to the quasi-Monte Carlo (Q-MC) approach.

The key element of our construction lies in distributing the node set in a deterministic way so that to guarantee low discrepancy between the desired and the obtained radial densities. This is achieved by a Q-MC analog of the *stratification* of Monte Carlo method [8]: nodes are distributed with piecewise constant (radial) density that approximates the desired one. We consider two different Q-MC sequences to draw from with (near-)constant radial density: irrational lattices and periodic Riesz minimizers. After dividing the set Ω into cube-shaped *voxels*, each voxel is filled with nodes obtained in one of the two ways, appropriately scaled, then the weighted s -energy of the whole node set is minimized. Although we discuss the radial density case in the present paper, an argument for the volumetric density can be produced along the same lines.

An *irrational lattice* (IL) here is defined as a discrete subset of the d -dimensional unit cube $[0, 1]^d$

$$(5) \quad \mathcal{L}_n = \left\{ \left(\text{frac}(C_1 + i/n), \text{frac}(i\alpha_1), \{i\alpha_2\}, \dots, \text{frac}(i\alpha_{d-1}) \right) : i = 1, \dots, n \right\},$$

where $\text{frac}(x) = \text{mod}(x, 1) = x - [x]$ denotes the fractional part of x , $C_1 > 0$ is fixed, and $\alpha_1, \alpha_2, \dots, \alpha_{d-1}$ are irrational numbers, linearly independent over the rationals. This terminology seems to be accepted in the low-discrepancy community [2], while closely related objects, when used for Q-MC purposes, are known as *Korobov/lattice point sets* [21].

The motivation for using an IL in this context comes in part from the desire to avoid recursive data structures, which can be detrimental to the overall performance, and in part is motivated by the existing results on the discrepancy of such lattices. It is known for example, that the two-dimensional ILs have the optimal order of L^2 discrepancy, [3], [2]. Furthermore, in all dimensions ILs are uniformly distributed [19, Chapter 1.6], that is, the fraction of lattice points inside any rectangular box with faces parallel to the coordinate planes converges to its volume. The simple linear structure of ILs makes them especially attractive for SIMD-parallelization.

Another Q-MC sequence that has proven to suit our purposes consists of *periodic Riesz minimizers* on the unit flat torus, that is, n -point collections $\mathcal{M}_n = \{\mathbf{x}_1, \dots, \mathbf{x}_n\}$ that minimize (2) on $([0, 1]^d)^n$ with the Euclidean distance $\|\cdot\|$ replaced by the periodic metric

$$(6) \quad \|\mathbf{x} - \mathbf{y}\|_{\sim}^2 = \Pi(x_1 - y_1) + \Pi(x_2 - y_2) + \Pi(x_3 - y_3),$$

where $\Pi(x) = \min(x^2, (1-x)^2)$, $0 \leq x \leq 1$. It follows from [17] that such configurations have optimal separation and asymptotically uniform volumetric density. It follows from the numerics also, that in this case the nearest neighbor distances vary very little from node to node; this and that minimizing configurations do not suffer from the lattice-like alignment, makes their rescaled copies good candidates for the stratification.

The number of nodes in individual voxels is defined by the function ρ , so the resulting collection has piecewise constant density; refining the voxel partition leads to an improved piecewise approximation of the desired (e.g., smooth) density. In practice, the dependence between the number of nodes contained in the unit cube, and average/minimal nearest neighbor distance is tabulated in advance, and then inverted during the construction of the node set.

3. THE ALGORITHM

The interested reader will find a Matlab codebase implementing the algorithm described here, as well as the sources for all the figures contained in the present paper, at [27].

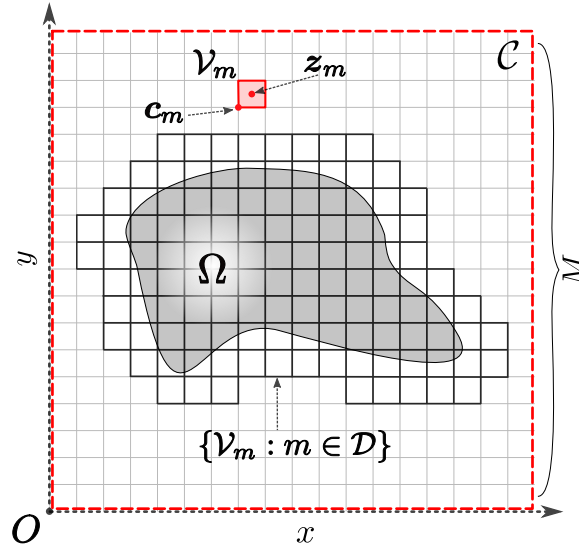


FIGURE 1. An illustration of some of the symbolic notation used in the algorithm below, in the case $d = 2$.

3.1. Formulation. If the nodes must be restricted to a certain compact set Ω , for example, support of a given indicator, we will refer to the set as *density support*, and to the indicator function as *point inclusion function*. We may further assume that Ω is contained in the d -dimensional unit cube $\mathcal{C} = [0, 1]^d$; the case of an arbitrary compact set then follows by choosing a suitable enclosing cube and applying scaling and translation. Suppose the radial density is prescribed by a Lipschitz-1 function; i.e., $|\rho(\mathbf{x}) - \rho(\mathbf{y})| \leq \|\mathbf{x} - \mathbf{y}\|$. The reason for this assumption is the respective property of

$\Delta(\mathbf{x})$, and is explained in further detail in the following section. Recall that we use an exponent $s > d$. We summarize the discussion in Section 2 into the following algorithm for generating nodes with radial density ρ :

Initial node layout.

- Step 0** Choose one of the two Q-MC sequences described in Section 2, $\{\mathcal{L}_n : n \geq 1\}$ or $\{\mathcal{M}_n : n \geq 1\}$, draw configurations with up to n_{\max} nodes from it, and determine the average nearest neighbor distance for its periodization by the integer lattice, denoted by $\bar{\Delta}_n$ for n nodes. Let $\lambda : (0, \infty) \rightarrow \{0, 1, 2, \dots, n_{\max}\}$ be the interpolated inverse to $\bar{\Delta}_n : \{1, 2, \dots, n_{\max}\} \rightarrow (0, 1]$.¹
- Step 1** Partition \mathcal{C} into M^d equal cube-shaped voxels of side length $1/M$, denoted by \mathcal{V}_m , $m = 1, \dots, M^d$, with faces parallel to the coordinate planes. Let $\{\mathcal{V}_m : m \in \mathcal{D}\}$ be the subset for which at least one of the adjacent (i.e., sharing a face) voxels has a vertex inside Ω .
- Step 2** Let $\bar{\rho}_m$ be the average value of ρ at the 2^d vertices of a voxel \mathcal{V}_m , $m \in \mathcal{D}$. Place inside \mathcal{V}_m a scaled and translated version of the n_m -point IL (5), or of the n_m -point periodic Riesz minimizer, using n_m defined by

$$n_m = \lambda(\bar{\rho}_m M).$$

Iterate over all $m \in \mathcal{D}$.

Saturation and cleanup.

- Step 3** Consider the voxels in $\{\mathcal{V}_m : m \in \mathcal{D}\}$, for which $\bar{\rho}_m M > 1$; at this stage they are empty. Sort such voxels by the increasing values of $\bar{\rho}_m$ and denote the resulting list $\{\mathcal{V}_m : m \in \mathcal{E}\}$. Iterate over $m \in \mathcal{E}$ and place a node in the center \mathbf{z}_m of every voxel satisfying $\Delta(\mathbf{z}_m) > \bar{\rho}_m$ (in practice, it suffices to only check distances to the previously selected \mathbf{z}_m with $m \in \mathcal{E}$, see discussion below).
- Step 4** For all nonempty voxels, remove nodes outside Ω .

Repel-type iterations, boundary detection.

- Step 5** Perform T iterations of the partial gradient descent on the weighted s -energy functional (3) with $\kappa(\mathbf{x}, \mathbf{x}) = c\rho(\mathbf{x})^s$, using the K nearest neighbors of each node: Let the initial configuration be the 0-th iteration, $\mathbf{x}_i^{(0)} = \mathbf{x}_i$, $i = 1, \dots, N$, with N denoting the total number of nodes distributed. On the t^{th} iteration, $1 \leq t \leq T$, given a node $\mathbf{x}_i^{(t)}$ with K nearest neighbors $\mathbf{x}_{j(i,k)}^{(t)}$, $k = 1, \dots, K$, form the weighted vector sum

$$\mathbf{g}_i^{(t)} = s\rho\left(\mathbf{x}_i^{(t)}\right)^s \sum_{k=1}^K \frac{\mathbf{x}_i^{(t)} - \mathbf{x}_{j(i,k)}^{(t)}}{\|\mathbf{x}_i^{(t)} - \mathbf{x}_{j(i,k)}^{(t)}\|^{s+2}},$$

the new node position can now be expressed as

$$(7) \quad \mathbf{x}_i^{(t+1)} = \begin{cases} \mathbf{x}_i^{(t)} + \frac{\Delta(\mathbf{x}_i^{(t)})}{t + C_2} \frac{\mathbf{g}_i^{(t)}}{\|\mathbf{g}_i^{(t)}\|} & \text{if this sum is inside } \Omega; \\ \mathbf{x}_i^{(t)}, & \text{otherwise,} \end{cases} \quad 1 \leq i \leq N.$$

where C_2 is a fixed offset chosen to control the step size between $\mathbf{x}_i^{(t)}$ and $\mathbf{x}_i^{(t+1)}$. If a “pullback” function is provided from a neighborhood of Ω to its boundary, the condition

¹Note that both ILs and the minimizers can have the nearest neighbor distance of at most 1, due to periodicity. We therefore take $\lambda(x) = 0$ whenever $x > 1$.

of $\mathbf{x}_i^{(t+1)}$ being inside Ω is replaced with applying the pullback; furthermore, if the radial density has an easily computable gradient, or is changing rapidly, an additional term must be included in (7) (see discussion below).

Update the neighbor indices $j(i, k)$ after every few iterations.

Step 6 If no boundary node set/pullback function is prescribed, define the boundary nodes as follows. Evaluate the point inclusion function for $\mathbf{x}_i \pm \Delta(\mathbf{x}_i)\mathbf{e}_l$, $l = 1, \dots, d$, $i = 1, \dots, N$, where \mathbf{e}_l is the l -th basis vector. If at least one such point lies outside Ω , the \mathbf{x}_i is considered to be a boundary node.

3.2. Discussion. Our assumption of ρ being Lipschitz-1 is natural, since $\Delta(\cdot)$ is always Lipschitz-1, if viewed as a function of position. To see this, consider any two nodes \mathbf{x}, \mathbf{y} , and let \mathbf{x}', \mathbf{y}' be their nearest neighbors, respectively, so that $\|\mathbf{x} - \mathbf{x}'\| = \Delta(\mathbf{x})$ and $\|\mathbf{y} - \mathbf{y}'\| = \Delta(\mathbf{y})$. It follows, $\Delta(\mathbf{x}) \leq \|\mathbf{x} - \mathbf{y}'\| \leq \|\mathbf{x} - \mathbf{y}\| + \Delta(\mathbf{y})$, which by symmetry implies Δ is Lipschitz-1.

Initial node layout. In the parts of the density support with constant ρ , the nodes will locally look like a periodization of the initial Q-MC sequence; hence the average neighbor distance in **Step 0** is tabulated for the periodized version.

If the IL sequence is chosen in **Step 0**, the n_m -node set placed in voxel \mathcal{V}_m at **Step 2** is an adjusted version of (5) as follows. Let for every \mathcal{V}_m the corner with the smallest absolute value be \mathbf{c}_m ; the points \mathbf{c}_m are then vertices of a lattice. Before scaling and translating \mathcal{L}_{n_m} , apply a random permutation to the coordinates of each node in it, so that to remove long-range lattice structure from the distribution; we will denote such an operation by σ . Then the IL in voxel \mathcal{V}_m becomes

$$(8) \quad \mathcal{L}'_{n_m} = \mathbf{c}_m + \frac{f}{M}\sigma(\mathcal{L}_{n_m}) + \frac{\mathbf{h}}{M},$$

where

$$f = 1 - c_d (n_{\max})^{-1/d}, \quad \mathbf{h} = \frac{1-f}{2} \cdot (1, 1, \dots, 1)^{\text{tr}},$$

with c_d depending only on the dimension. The quantities f and \mathbf{h} ensure that the lattice points in \mathcal{L}_m are inset into the voxel by about half the separation distance, avoiding poorly separated points along the voxel interfaces.

When the periodic minimizer sequence is selected in **Step 0**, the inset is defined in a similar way, but the permutation is just an identity, $\sigma \equiv \text{id}$, as the minimizers don't have the lattice structure. Likewise, the scaling factor and translation are

$$f_m = 1 - c_d (n_m)^{-1/d}, \quad \mathbf{h}_m = \frac{1-f_m}{2} \cdot (1, 1, \dots, 1)^{\text{tr}}.$$

The analog of (8) thus takes the form

$$(9) \quad \mathcal{M}'_{n_m} = \mathbf{c}_m + \frac{f_m}{M}\mathcal{M}_{n_m} + \frac{\mathbf{h}_m}{M}.$$

As one would expect, the average separation for the sequence $\{\mathcal{M}_n\}$ is larger than that of $\{\mathcal{L}_n\}$ for the respective values of n . While the inset for the latter is necessary to account for the node proximity after periodization, for the former it serves to mitigate the effects of interfacing voxels containing different number of nodes. This is further discussed in the Appendix.

Saturation and cleanup. Observe that in **Step 2** the nodes are only placed in \mathcal{V}_m 's for which either of the adjacent voxels has corners inside the density support Ω . This means, removing the nodes outside the support in **Step 4** does not lead to much overhead. Furthermore, since the density is evaluated at the corners only and not at individual nodes, the total number of evaluations may be significantly reduced, which is especially useful when ρ is computationally expensive. This is of course possible due to Lipschitz-1 nature of ρ . One could equally use a different arrangement of nearby corners to detect whether to count a particular voxel as being inside/outside the support.

The fact that the greedy node selection from $\{\mathcal{V}_m : m \in \mathcal{E}\}$ in **Step 3** requires only checking the separation from nodes in the list \mathcal{E} itself can be justified as follows. Assume that the radial density satisfies $\rho(\mathbf{z}_m) = 1 + D$ for some $m \in \mathcal{E}$, $D > 0$; then the distance $\|\mathbf{z}_m - \mathbf{x}\|$ for any \mathbf{x} with $\rho(\mathbf{x}) \leq 1$ is at least D due to the Lipschitz-1 property. Furthermore, nodes in voxels with large values of $\bar{\rho}_m M$ are located close to the center, therefore at least at the distance $0.5 + D$ from our \mathbf{z}_m . Leaving empty the centers with radial density from 1 up to $1 + D$ for $D \approx 0.3$, since these must be close to the parts of \mathcal{C} with low values of ρ anyway, where there are neighboring nodes from **Step 2**, we obtain that in the sparser parts, the ratio $\rho(\mathbf{x})/\Delta(\mathbf{x})$ is at most $(1 + D)/(0.5 + D) \leq 1.625$ for $D \geq 0.3$. Applying the partial gradient descent in **Step 5**, we are able to further bring this ratio closer to 1.

Repel-type iterations, boundary detection. The equality $\kappa(\mathbf{x}, \mathbf{x}) = c\rho(\mathbf{x})^s$ can be justified by observing that each node \mathbf{x} of the target distribution must be contained in a ball of radius $\rho(\mathbf{x})$, not containing any of the other nodes, hence, the volumetric density must be inverse proportional to $\rho(\mathbf{x})^d$. On the other hand, minimizers of (3) converge to the distribution with volumetric density $\kappa(\mathbf{x}, \mathbf{x})^{-d/s}$; hence $\kappa(\mathbf{x}, \mathbf{x})^{d/s} = c\rho(\mathbf{x})^d$.

The vector sum in **Step 5** corresponds to one of the terms of the gradient of the weighted Riesz s -energy; the complete gradient of a single summand of the s -energy $e(\mathbf{x}, \mathbf{y}) = \kappa(\mathbf{x}, \mathbf{y})\|\mathbf{x} - \mathbf{y}\|^{-s}$ is equal to

$$\nabla_{\mathbf{x}} e(\mathbf{x}, \mathbf{y}) = -s \kappa(\mathbf{x}, \mathbf{y})(\mathbf{x} - \mathbf{y})\|\mathbf{x} - \mathbf{y}\|^{-s-2} + \nabla_{\mathbf{x}} \kappa(\mathbf{x}, \mathbf{y})\|\mathbf{x} - \mathbf{y}\|^{-s}.$$

In practice, there will be no isolated nodes, so the node \mathbf{y} here is close to \mathbf{x} , and, since the off-diagonal values of $\kappa(\mathbf{x}, \mathbf{y})$ do not influence the limiting distribution (for details see [5]), we assume $\kappa(\mathbf{x}, \mathbf{y}) \approx \kappa(\mathbf{x}, \mathbf{x})$ to rewrite the previous equation as

$$(10) \quad \nabla_{\mathbf{x}} e(\mathbf{x}, \mathbf{y}) = -s \rho(\mathbf{x})^s (\mathbf{x} - \mathbf{y})\|\mathbf{x} - \mathbf{y}\|^{-s-2} + s \nabla_{\mathbf{x}} \rho(\mathbf{x}) \rho(\mathbf{x})^{s-1} \|\mathbf{x} - \mathbf{y}\|^{-s}.$$

The ratio of the second to the first term is bounded by $\nabla_{\mathbf{x}} \rho(\mathbf{x})\|\mathbf{x} - \mathbf{y}\|/\rho(\mathbf{x})$ and, provided that the distances from \mathbf{x} to its nearest neighbors are close to the value of $\rho(\mathbf{x})$, is at most $c \nabla_{\mathbf{x}} \rho(\mathbf{x})$ for a constant c . This condition is satisfied because the chosen Q-MC sequences have very regular local structure. In practice, the node distance is small on the scale of the support and varies slowly, so the second term will have negligible impact on the direction of the gradient after normalization; besides, precise gradient computation may prove costly. For these reasons we omit the second term in equation (7). If it is necessary to deal with a fast-changing radial density, a trade-off between the computational costs and the resulting distribution properties must be sought.

It doesn't matter which minimization method is applied to the weighted s -energy, rather the gradient descent is chosen due to its simplicity. Note, the second case in (7), leading to shrinking of the line stepping distance, can be thought of as a simplistic backtracking line search; it turns out to be sufficient for our purposes. Furthermore, applying a more involved line search may significantly deplete performance for complicated or nonsmooth domains.

The values of K and T can be adjusted to achieve a trade-off between execution speed/memory consumption and local separation. In our experiments,² even relatively small values of K and T produce good results: we used $K \approx T \approx 30$ for 1.3 million nodes in Section 4.1, and $K \approx T \approx 20$ for about 250 thousand nodes in Section 4.2.

4. SAMPLE APPLICATIONS

4.1. Atmospheric node distribution using surface data. We use the geodata [1] from the collection of global relief datasets produced by NOAA (National Oceanic and Atmospheric Administration), which contains a 1 arc-minute resolution model. We generate a sample configuration consisting of 1,356,566 nodes distributed uniformly inside an atmospheric-type shell Ω_{etopo} : the outer boundary of Ω_{etopo} is spherical, the inner one is an interpolation of the relief from ETOPO1 data, exaggerated by a factor of 100. The scale is chosen so that the average Earth radius, assumed to be 6,371,220 meters, has unit length; the radius of the outer boundary is set to 1.1, which corresponds to the height of 6,371 meters above the average radius, given the exaggeration factor.

The ETOPO1 dataset stores relief as a 21 600-by-10 800 array of elevations above the sea level; equivalently, of radial coordinates that correspond to the spherical angles defined by the array's indices. The data points are equispaced on lines of constant azimuth/inclination with angular distance $B = \pi/10\,800$ between them. To determine whether a given node $\mathbf{x} = (r_{\mathbf{x}}, a_{\mathbf{x}}, p_{\mathbf{x}})$ belongs to Ω_{etopo} , its radial coordinate $r_{\mathbf{x}}$ was compared with a linear interpolation of the values of radii of three ETOPO1 points with the nearest spherical coordinates. For example, assume that such three points have the spherical coordinates (r_j, a_j, p_j) , $j = 1, 2, 3$, where $0 \leq a \leq 2\pi$ and $0 \leq p \leq \pi$ are the azimuth and polar angle, respectively, and

$$\begin{aligned} a_1 = lB, \quad a_2 = (l+1)B, \quad a_3 = lB, \quad 0 \leq l \leq 21\,599; \\ p_1 = mB, \quad p_2 = mB, \quad p_3 = (m+1)B, \quad 0 \leq m \leq 10\,799. \end{aligned}$$

Without loss of generality, the inequalities

$$lB \leq a_{\mathbf{x}} < (l+1)B; \quad mB \leq p_{\mathbf{x}} < (m+1)B$$

hold true. The point inclusion function is defined in this case as

$$\chi(\mathbf{x}; \Omega_{\text{etopo}}) = \begin{cases} 1, & r_1 + \frac{a_{\mathbf{x}} - a_1}{B}(r_2 - r_1) + \frac{p_{\mathbf{x}} - p_1}{B}(r_3 - r_1) < r_{\mathbf{x}} < 1.1; \\ 0, & \text{otherwise,} \end{cases}$$

with 1.1 being the radius of the outer sphere in the chosen scale. In effect, the algorithm for evaluating the $\chi(\cdot; \Omega_{\text{etopo}})$ described here coincides with the star-shaped point location algorithm from [24, Section 2.2], applied to the interpolated Earth surface and the outer spherical boundary.

Our node set consists of 1,356,566 nodes with the nearest-neighbor separation close to the constant $\rho(\mathbf{x}) = 0.01124$, and our top priority was to ensure the low variance of the radial separation across the configuration, especially on the surface. The time required to draw the initial configuration from a piecewise IL and localize it inside Ω_{etopo} , corresponding to **Step 0-Step 4** of the algorithm, was 6.37 seconds on a common laptop with an *Intel i5* CPU. We used the golden-ratio derived parameters α_1, α_2 , listed first in Figure 10. Performing 29 iterations in **Step 5** with $K = 33$ nearest neighbors for the whole 1.3M-node set took additional 200.60 seconds. Several statistics of the

²The Matlab code we provide performs naive autotuning of K and T , using the total number of nodes to be placed. Although sufficient for demonstration purposes, there is room for improvement.

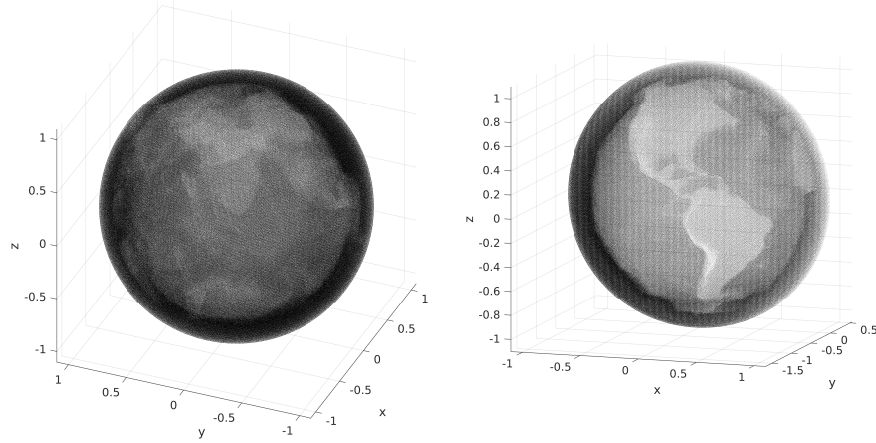


FIGURE 2. Left: a general view of a uniform node distribution in an atmospheric-like shell. Right: a separate view of the Western hemisphere.

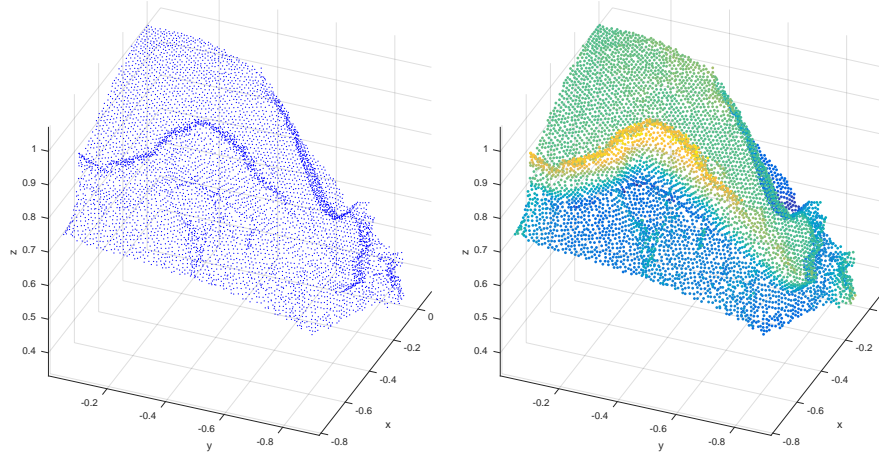


FIGURE 3. Surface subset: a fragment of the Western coast of South America. The nodes on the right are color-coded using heights.

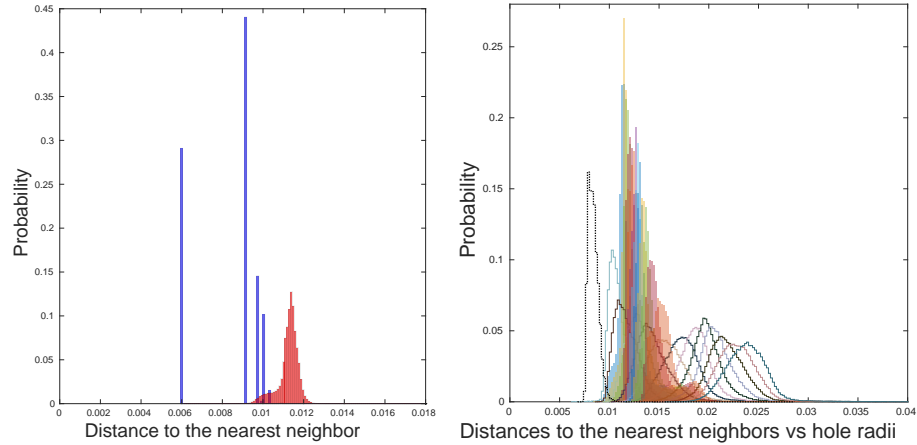


FIGURE 4. The effects of the repel procedure and hole radii. Left: probability distribution of the nearest-neighbor distances in the atmospheric node set, before (blue) and after (red) executing the repel subroutine. Right: distribution of distances to the 12 nearest neighbors for the whole configuration (color only), for the surface subset (contours), the hole radii (black dashed contour on the left).

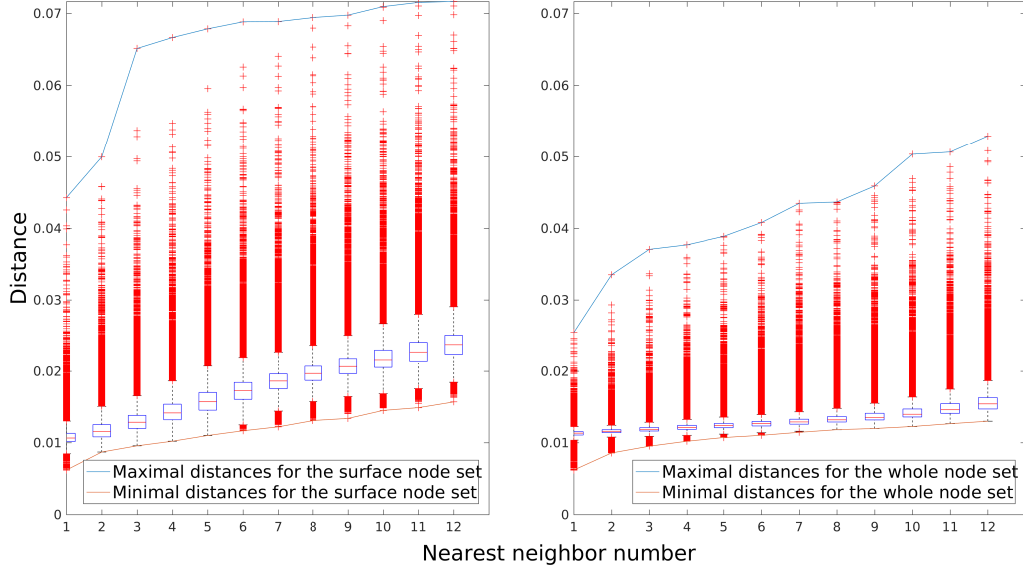


FIGURE 5. Distribution of distances to the 12 nearest neighbors for the atmospheric node configuration; medians and the 25th and 75th percentiles are shown. Left: the surface subset. Right: the whole set. Scales are the same in both subplots.

resulting set are presented in the following table; here again we used the common notation \bar{x} for the averaged value of a quantity x . Notation Δ^k stands for the distance to the k -th nearest neighbor.

	Whole node set	Surface nodes
$\overline{\Delta^{12}(\mathbf{x})/\Delta^2(\mathbf{x})}$	1.3674	2.0353
$\overline{\Delta^4(\mathbf{x})/\Delta^1(\mathbf{x})}$	1.0859	1.34019
99th percentile of $\{\Delta(\mathbf{x}_i)\}$	0.012143	0.014444
$\overline{\Delta(\mathbf{x})}$	0.011243	0.010879
1st percentile of $\{\Delta(\mathbf{x}_i)\}$	0.009652	0.009340

Figure 3 illustrates the distribution of nodes close to the surface of Ω_{etopo} . No pullback function has been used, just the inclusion check performed as in (7). Observe that the near-surface nodes display no artifacts, and the spacing does not significantly depend on the local surface shape. The left subplot in the Figure 4 illustrates the effect of **Step 5** on the distribution of distances to the nearest neighbor. In the right subplot, we have collected distances to the 12 nearest neighbors for the whole configuration, and separately for the surface subset. The histogram also contains the distribution of *hole radii*, that is, distances from the Voronoi centers of the entire node configuration to their respective nearest nodes. It is a well-known fact that the Voronoi centers are local maxima of the distance from the node set [11], considered as a function on the whole space \mathbb{R}^3 . Note that all the histograms on the right are normalized by probability, not by the node count.

The pair of plots in Figure 5 shows in detail the distribution of distances to the nearest neighbors in the sample node set. It has been produced using the standard Matlab routine *boxplot*. For each of the blue boxes corresponding to a specific nearest neighbor, the central mark is the median, the edges of the box denote the 25th and 75th percentiles. The red crosses mark outliers.

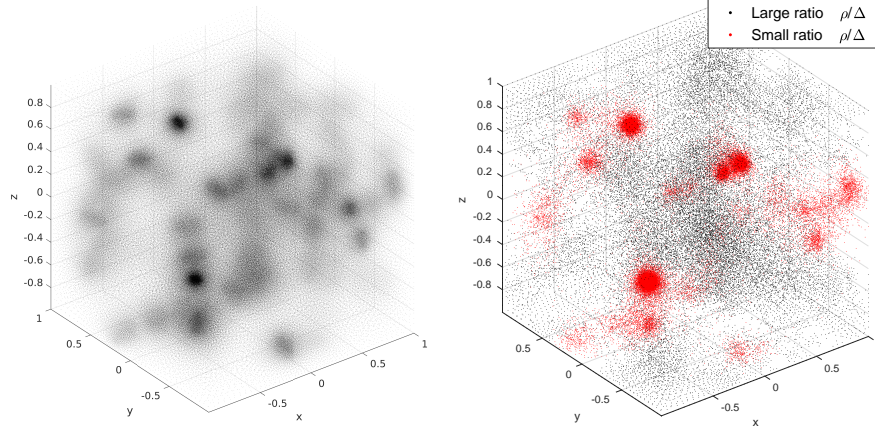


FIGURE 6. Left: the node set from Section 4.2. Right: node locations that contribute to the distribution of the ratio $\rho(\mathbf{x})/\Delta(\mathbf{x})$ beyond the top and bottom 5-percentiles.

4.2. Point cloud. To demonstrate a nonuniform node distribution using our algorithm, we fix a collection of 100 points, \mathcal{P}_{100} , inside the cube $[-1, 1]^3$, and consider the following radial density function:

$$\rho(\mathbf{x}) = (\Delta(\mathbf{x}; \mathcal{P}_{100}) + \Delta^2(\mathbf{x}; \mathcal{P}_{100})) / 20,$$

where, as above, Δ^k is the distance to the k -th nearest neighbor. A possible interpretation of this density is a distribution that concentrates about a set of points \mathcal{P}_{100} , which are of particular interest for a certain model.

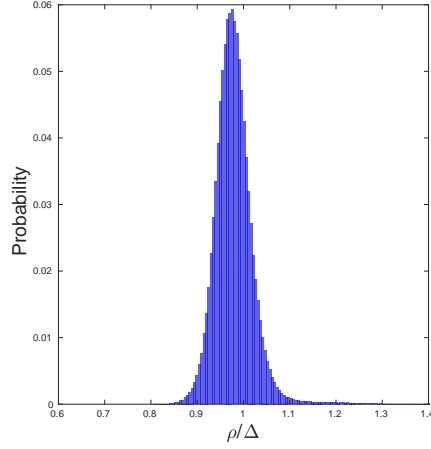
We proceed as in the algorithm in Section 3.1, not using the additional gradient term described in Section 3.2. Still, the resulting distribution recovers the density function quite well. Picking 577,321 nodes from the sequence $\{\mathcal{L}_n\}$ took 3.80 seconds on a dedicated machine with an 8-core *Intel Xeon* CPU; performing 200 iterations in **Step 5** with $K = 30$ nearest neighbors took about 800 seconds.

Figure 7 contains the distribution of the ratio $\rho(\mathbf{x})/\Delta(\mathbf{x})$. The minimal and maximal values of the ratio are about 0.8099 and 1.8231 respectively; its mean value is 0.9797, and the variance is 0.0019. The bottom and top 5-percentiles are 0.9208 and 1.0441, respectively.

4.3. Spherical shell. The motivation for this example comes from atmospheric modeling. Representing the Earth surface by a sphere, we consider first a thin 3-dimensional shell Ω_{shell} of inner radius R_{inner} and outer radius $R_{\text{inner}} + H_{\text{atm}}$ with constant target separation h between points in the radial (vertical) direction, and the tangential (horizontal) separation to be $\tau(r) = C \cdot r$ at radius r , for some constant C . With typical choices of parameters, τ will be much larger than h , reflecting the much higher resolution needed in the vertical direction due to $H_{\text{atm}} \ll R_{\text{inner}}$. We make a radial change of variables, which can be written in spherical coordinates as $(r, a, p) \rightarrow (\hat{r}(r), a, p)$, so that any configuration in Ω_{shell} having the 2-directional resolutions $\tau(r)$ and h will have isotropic resolution after the transformation. It is much easier to construct RBF bases in the isotropic case, hence our deliberation.

Following this change of variables, the radial/tangential node separations become, respectively,

$$(11) \quad \begin{aligned} \hat{\nu}(r) &= h \cdot \hat{r}'(r) \\ \hat{\tau}(r) &= C \cdot \hat{r}(r). \end{aligned}$$

FIGURE 7. Distribution of the ratios $\rho(\mathbf{x})/\Delta(\mathbf{x})$ for the node set in Section 4.2.

Setting these two quantities to be equal, we obtain the ODE

$$\hat{r}'(r) = \frac{C}{h} \cdot \hat{r}(r)$$

with initial condition $\hat{r}(R_{\text{inner}}) = 1$, and its solution becomes

$$\hat{r}(r) = \exp\left(C \cdot \frac{r - R_{\text{inner}}}{h}\right).$$

From the second equation in (11) follows that our goal is to generate a node set in the (\hat{r}, a, p) -space, whose separation is proportional to \hat{r} and is equal in all directions: $\rho(\mathbf{x}) = C \cdot \|\mathbf{x}\|$. The outer radius of the image of Ω_{shell} in the (\hat{r}, a, p) -space is a function of R_{inner} and H_{atm} ; our model implies $R_{\text{inner}} = 6,371,220$, the mean radius of the Earth in meters, and $H_{\text{atm}} = 12,000$, the thickness of the atmospheric layer we are interested in. The constant C is determined by the desired tangential separation at the $r = R_{\text{inner}}$ level.

Say, we intend to generate nodes corresponding to the 2 degree resolution on the spherical “Earth surface” and $h = 400$ meter vertical resolution. Due to the peculiarities of atmospheric modeling, we would like to fix two much denser sets of nodes on the inner and outer boundary of Ω_{shell} ; specifically, we are using 12,100 approximate Riesz energy minimizers on a sphere, appropriately rescaled. The interior nodes are generated using our algorithm, and then **Step 5** is modified so that to leave the boundary subset intact. This, however, causes a difficulty: the separation distances between the interior and the surface nodes must remain large; on the other hand, our generic formulation of **Step 5** does not account for the much higher concentration of nodes on the surface, which causes excessive repelling force, seen in the oscillations of the radial distribution, Figure 9. Mitigating this effect requires artificially weakening the repulsive force caused by the boundary nodes, a straightforward task using our codebase. Instead, we will describe here the performance of the generic algorithm, to show the complications that may arise when applying it to specialized problems.

Drawing 358,915 nodes from the sequence $\{\mathcal{M}_n\}$ took only 0.58 seconds on the same machine as in Section 4.2; performing 200 repel steps with 30 nearest neighbors further took about 120 seconds. The left subplot in Figure 9 contains the distribution of the ratio $\rho(\mathbf{x})/\Delta(\mathbf{x})$. The minimal and

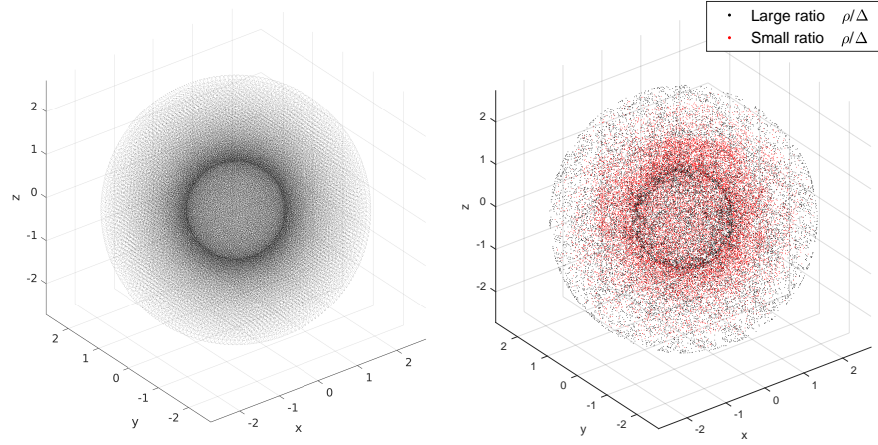


FIGURE 8. Left: the node set from Section 4.3. Right: node locations that contribute to the distribution of the ratio $\rho(\mathbf{x})/\Delta(\mathbf{x})$ beyond the top and bottom 5-percentiles.

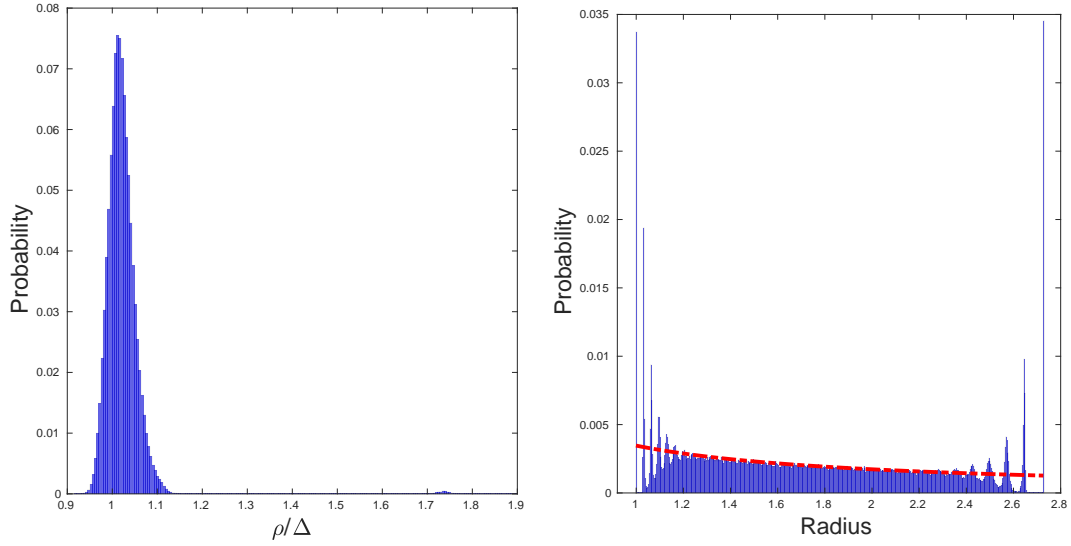


FIGURE 9. Left: Distribution of the ratios $\rho(\mathbf{x})/\Delta(\mathbf{x})$ for the node set in Section 4.3. Right: Radial node distribution, actual (blue) and the theoretic (red) continuous component; i.e., without the δ -function spikes at the endpoints.

maximal values of the ratio are about 0.9165 and 1.8989 respectively; its mean value is 1.0226, and the variance is 0.0024. The bottom and top 5-percentiles are 0.9782 and 1.0717, respectively.

Finally, it is important to note that domain Ω_{shell} can be challenging for the basic form of our algorithm, as described in Section 3.1: obtaining satisfying convergence requires using the full version of gradient descent (10). The reasons for Ω_{shell} being more difficult to tackle than, say, example in Section 4.2, are that due to convexity of the outer boundary, the weighted s -energy minimizers on it are denser than on the sphere with radius $\hat{r}(R_{\text{inner}} + H_{\text{atm}}) - 10^{-3}$, for example; see also discussion

at the end of Section 2.1. Getting rid of the artifacts at the endpoints of the radial distribution is obtained through using the full gradient, weakening the repulsion of the fixed boundary nodes, and *not* striving for the full convergence of a minimization method applied to the Riesz energy.

5. CONCLUDING REMARKS

- Our algorithm has proven very efficient for slowly varying radial densities, that are relatively small compared to the entire node set scale, and is capable of handling very complex underlying sets.
- Of the two Q-MC sequences we considered, the periodic Riesz minimizers appear more promising, being devoid of the lattice structure and having high space utilization. On the other hand, we have successfully applied ILs as an elementary uniform configuration. One could use different sets of irrational parameters $\alpha_1, \dots, \alpha_{d-1}$ for different numbers of nodes in a voxel. Although this might be useful in mitigating the non-isotropic behavior of ILs, it makes hard to control node separation at voxel interfaces.
- Our approach is applicable to higher dimensions just as well: the Riesz-energy approach is largely (with a proper value of s) dimension-agnostic. A shortcoming that is common to all quasi-Monte Carlo methods (and their derivatives) is, however, a much worse performance (measured by L^2 discrepancy), compared to Monte-Carlo distribution, in dimensions starting at about 15 [8].
- Our algorithm acts very locally, and it therefore must be straightforward to add multi-resolution and adaptive refinement, as is widely done for grids [10], [12], yet as of this writing, our proof-of-concept implementation does not include these features. Still, we would like to observe that refining the voxel structure is indeed easier than refining a mesh, since no geometry is taken into account.
- The closest set of goals to what we have presented here, that we're aware of, is posed in the pioneering paper [26]; our method is crafted for full-dimensional domains, and apparently performs faster in this case. The bubble packing algorithm in [26] is morally similar to the greedy filling of centers in **Step 3**, while physical relaxation is an alternative to the energy minimization we employ; of course, the idea of relaxation can also be found in a number of related references, and is a well-known approach in this context, see for example [23].
- Our method requires computing the gradient of the desired radial density in the cases when the outer boundary of the underlying set is uniformly convex, and/or when the radial density changes quickly. Alternatively, fine partition of the set is necessary. Either solution, however, may be computationally expensive.

6. APPENDIX: SEPARATION PROPERTIES OF SEQUENCES $\{\mathcal{L}_n\}$ AND $\{\mathcal{M}_n\}$

This Appendix deals with the results of our numerical experiments, set in the 3-dimensional space. The function $\lambda(r)$ used in **Step 2** is the number of nodes in the unit cube $[0, 1]^3$, placed according to (5), or obtained by minimizing the Riesz s -energy (2) with periodic metric, such that the mean separation distance of these nodes is the closest to r . To compute $\lambda(r)$ for the periodization of $\{\mathcal{L}_n\}$, we tabulate mean separations $\bar{\Delta}_n$ in a sample configuration comprising \mathcal{L}_n and its $26 = 3^3 - 1$ copies, obtained translating \mathcal{L}_n by the vectors $\{(i, j, k)^{\text{tr}} : i, j, k \in \{0, \pm 1\} \text{ and } |i| + |j| + |k| > 0\}$. The tabulated dependence of separation on n is then inverted and interpolated using a piecewise cubic Hermite interpolating polynomial. The reason to consider separation distance between configurations in 3^d cubes in dimension d (and not a single cube with a single instance of \mathcal{L}_n) is to account for the boundary effects. Likewise, to compute $\lambda(r)$ for the Riesz minimizers, the mean separation of \mathcal{M}_n is tabulated for $1 \leq n \leq n_{\text{max}}$, then the inverse dependence is interpolated. No copies of \mathcal{M}_n are

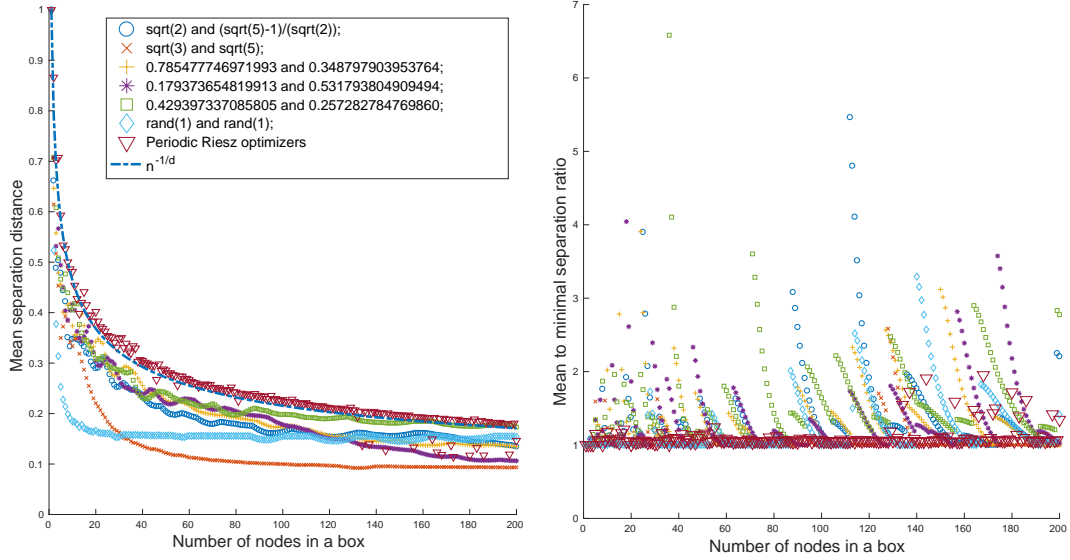


FIGURE 10. Left: dependence of the mean separation distances on the number of nodes in the unit cube for different values of parameters α_1, α_2 ; the $n^{-1/d}$ decay rate shown as a dash-dot line. Right: ratios of the mean separation distances to the minimal ones for the same configurations.

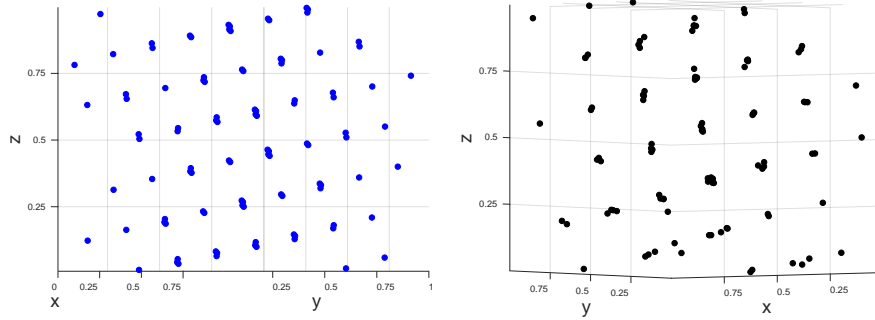


FIGURE 11. Left: A cross-section of the IL \mathcal{L}_{100} with parameters 0.179373654819913 and 0.531793804909494. Right: A (different) cross-section of \mathcal{M}_{100} .

considered alongside the original configuration, since periodicity condition is already included in the metric (6).

In general, putting too many nodes in individual voxels is justified only if the radial density function ρ varies slowly. For our applications, $n_{\max} \leq 100$ was sufficient. The left plot in Figure 10 illustrates the delicate dependence of the separation distances of ILs on the irrational parameters. While any set of irrational quantities $\alpha_1, \dots, \alpha_{d-1}$ in (5) that are linearly independent over rationals will give a uniformly distributed IL as n grows, certain values may perform better than the others. In particular, adjustments can be made to improve the distribution for small values of n . For example, it is known from [2] that a 2-dimensional IL generated by the golden ratio has optimal L^2 discrepancy. Numerical experiments have shown that its 3-dimensional analog with parameters $\alpha_1 = \sqrt{2}$, $\alpha_2 = (\sqrt{5} - 1)/\sqrt{2}$ does perform well for large numbers of nodes; yet by carrying out a

Monte Carlo search for the parameters maximizing separation distance in (5), we found several (necessarily rational) pairs that performed at least just as well for up to $n = 200$.

Curiously enough, a pair of random numbers drawn uniformly from $[0, 1]$ (shown in the legend as `rand(1)`), consistently performed better than the pair $\sqrt{3}$ and $\sqrt{5}$, starting at $n \approx 40$. We were able to reproduce this behavior in a number of runs; in fact, we haven't seen a random pair that wouldn't always outperform $\sqrt{3}$ and $\sqrt{5}$ after a fairly small n .

The second graph in Figure 10 shows the ratios of the mean to minimal separation distances $\bar{\Delta}_n/\Delta_n$ for the same range of n . In both subfigures, Riesz periodic minimizers clearly stand out, by having the largest mean separation (left), and by smallest ratios (right). This means, the nearest neighbor distances $\Delta(\mathbf{x})$ vary little from node to node in the $\{\mathcal{M}_n\}$ sequence. We conclude this section by presenting a pair of cross-sections of the IL \mathcal{L}_{100} and the configuration \mathcal{M}_{100} that look remarkably similar. In fact, we found the vague resemblance between the low-energy periodic configurations and lattice structures, similar to ILs, quite interesting, given the connection between packing and Riesz energy minimization [17], and that the highest packing density in the 3-dimensional space is achieved, in particular, by the hcp lattice [11].

ACKNOWLEDGEMENTS

O.V. and T.M. were supported, in part, by the NSF grant DMS-1516400.

REFERENCES

- [1] C. Amante and B. W. Eakins. ETOPO1 1 Arc-Minute Global Relief Model: Procedures, Data Sources and Analysis. <https://doi.org/10.7289/V5C8276M>, 2009.
- [2] D. Bilyk. The L^2 discrepancy of irrational lattices. In *Monte Carlo and Quasi-Monte Carlo Methods 2012*, pages 289–296. Springer, 2013.
- [3] D. Bilyk, V. N. Temlyakov, and R. Yu. The L^2 Discrepancy of Two-Dimensional Lattices. In *Springer Proc. Math. Stat.*, volume 25, pages 63–77. 2012.
- [4] S. V. Borodachov, D. P. Hardin, and E. B. Saff. Asymptotics for discrete weighted minimal Riesz energy problems on rectifiable sets. *Trans. Amer. Math. Soc.*, 360(3):1559–1580, 2008.
- [5] S. V. Borodachov, D. P. Hardin, and E. B. Saff. Low Complexity Methods For Discretizing Manifolds Via Riesz Energy Minimization. *Found. Comput. Math.*, 14(6):1173–1208, 2014.
- [6] J. S. Brauchart, A. B. Reznikov, E. B. Saff, I. H. Sloan, Y. G. Wang, and R. S. Womersley. Random point sets on the sphere—hole radii, covering, and separation. *Experimental Mathematics*, pages 1–20, 2016.
- [7] D. Broomhead, D. S. and Lowe. Multivariable Functional Interpolation and Adaptive Networks. *Complex Syst.*, 2:321–355, 1988.
- [8] R. E. Caflisch. Monte Carlo and quasi-Monte Carlo methods. *Acta Numerica*, 7:1, 1998.
- [9] C. Chang and C. Lin. LIBSVM. *ACM Trans. Intell. Syst. Technol.*, 2(3):1–27, 2011.
- [10] Clawpack Development Team. Clawpack software, 2017. Version 5.4.0.
- [11] J. H. Conway and N. J. A. Sloane. *Sphere packings, lattices and groups*, volume 290 of *Grundlehren der Mathematischen Wissenschaften [Fundamental Principles of Mathematical Sciences]*. Springer-Verlag, New York, third edition, 1999. With additional contributions by E. Bannai, R. E. Borcherds, J. Leech, S. P. Norton, A. M. Odlyzko, R. A. Parker, L. Queen and B. B. Venkov.
- [12] L. Debreu, C. Voulard, and E. Blayo. AGRIF: Adaptive grid refinement in fortran. *Computers & Geosciences*, 34(1):8–13, 2008.
- [13] B. Fornberg. *A practical guide to pseudospectral methods*. Cambridge University Press, 1996.
- [14] B. Fornberg and N. Flyer. *A Primer on Radial Basis Functions with Applications to the Geosciences*. Society for Industrial and Applied Mathematics, Philadelphia, PA, 2015.
- [15] B. Fornberg and N. Flyer. Fast generation of 2-D node distributions for mesh-free PDE discretizations. *Comput. Math. with Appl.*, 69(7):531–544, 2015.
- [16] B. Fornberg and N. Flyer. Solving PDEs with radial basis functions. *Acta Numerica*, 24:215–258, 2015.
- [17] D. P. Hardin and E. B. Saff. Minimal Riesz Energy Point Configurations for Rectifiable d-Dimensional Manifolds. *Adv. Math.*, 193(1):174–204, 2003.

- [18] D. P. Hardin, E. B. Saff, and O. V. Vlasniuk. Generating Point Configurations via Hypersingular Riesz Energy with an External Field. *SIAM J. Math. Anal.*, 49(1):646–673, 2017.
- [19] L. Kuipers and H. Niederreiter. *Uniform distribution of sequences*. Dover Publications, Mineola, N.Y., 2006.
- [20] N. S. Landkof. *Foundations of modern potential theory*, volume 180. Springer, 1972.
- [21] C. Lemieux. *Monte Carlo and Quasi-Monte Carlo Sampling*. Springer Series in Statistics. Springer New York, New York, NY, 2009.
- [22] J. J. Monaghan. Why particle methods work. *SIAM J. Sci. Statist. Comput.*, 3(4):422–433, 1982.
- [23] P.-O. Persson and G. Strang. A Simple Mesh Generator in MATLAB. *SIAM Rev.*, 46(2):329–345, jan 2004.
- [24] F. P. Preparata and M. I. Shamos. *Computational Geometry*. Springer New York, 1985.
- [25] V. Shankar, G. B. Wright, R. M. Kirby, and A. L. Fogelson. A radial basis function (RBF)-finite difference (FD) method for diffusion and reaction–diffusion equations on surfaces. *Journal of Scientific Computing*, 63(3):745–768, 2014.
- [26] K. Shimada and D. C. Gossard. Bubble mesh. In *Proc. third ACM Symp. Solid Model. Appl. - SMA '95*, pages 409–419, New York, New York, USA, 1995. ACM Press.
- [27] O. Vlasniuk and T. Michaels. Boxed lattices and Riesz minimizers for RBF computations. <https://github.com/OVlasniuk/3dRBFnodes.git>, 2017. [Online; accessed 12-October-2017].
- [28] H. Wendland. *Scattered Data Approximation*. Cambridge University Press, 2004.